A Calibration Method for Fully Polarimetric Microwave Radiometers

Janne Lahtinen, *Student Member, IEEE*, A. J. Gasiewski, *Fellow, IEEE*, Marian Klein, and Ignasi S. Corbella, *Member, IEEE*

***Abstract*—A technique for absolute end-to-end calibration of a fully polarimetric microwave radiometer is presented. The technique is based on the tripolarimetric calibration technique of Gasiewski and Kunkee, but is extended to provide a means of calibrating all four Stokes parameters. The extension is facilitated using a biaxial phase-retarding microwave plate to provide a precisely known fourth Stokes signal from the Gasiewski–Kunkee (GK) linearly polarized standard. The relations needed to determine the Stokes vector produced by the augmented standard are presented, and the effects of nonidealities in the various components are discussed. The application of the extended standard to determining the complete set of radiometer constants (the calibration matrix elements) for the National Oceanic and Atmospheric Administration Polarimetric Scanning Radiometer in a laboratory environment is illustrated. A calibration matrix inversion technique and error analysis are described, as well. The uncertainties associated with practical implementation of the fully polarimetric standard for spaceborne wind vector measurements are discussed relative to error thresholds anticipated for wind vector retrieval from the U.S. National Polar-Orbiting Environmental Satellite System.**

***Index Terms*—Calibration, dielectric devices, error analysis, microwave radiometry, polarimetry, remote sensing, wind.**

I. Introduction

DURING the past decade, there has been an increasing interest in passive polarimetric microwave remote sensing for airborne and spaceborne earth applications, in particular for maritime wind vector measurement. Several studies have elucidated this capability, beginning with airborne experiments revealing ocean surface emission anisotropies by Etkin *et al.* [1], followed later by corroborating measurements from Irisov *et al*. [2] and Yueh *et al*. [3]. The inversion of polarimetric ocean microwave emission anisotropies for one- and two-dimensional ocean wind vector imaging was first demonstrated by Piepmeier and Gasiewski [4] via using tripolarimetric measurements at 10.7 and 37 GHz. From these studies, it has become clear that new and useful information can be obtained on ocean surface anisotropies using measurements of the third and fourth Stokes parameters within microwave window channels. Third and fourth Stokes parameter measurements are also potentially valuable for vertical sounding of mesospheric thermal structure [5], an application that is anticipated to provide valuable climatic information, and for interference detection in passive microwave radiometry.

The complete second-order spectral characterization of electromagnetic waves requires a total of four parameters at any given frequency: two parameters to represent the rms power within two orthogonal modes (e.g., vertical and horizontal linear, as in the modified Stokes parameter basis [6, p. 125]) and two additional parameters to represent the complex coherence between these two modes. To express the polarimetric characteristics of these stochastic transverse wave processes, we can use the full (modified) Stokes vector under the Rayleigh–Jeans approximation

$$\overline{T}_B = \begin{bmatrix} T_v \\ T_h \\ T_3 \\ T_4 \end{bmatrix} = \begin{bmatrix} T_v \\ T_h \\ T_{45} - T_{-45} \\ T_{\rm cl} - T_{\rm cr} \end{bmatrix} = \frac{\lambda^2}{k_B \cdot \eta} \begin{bmatrix} \langle |E_v|^2 \rangle \\ \langle |E_h|^2 \rangle \\ 2{\rm Re}\langle E_v E_h^* \rangle \\ 2{\rm Im}\langle E_v E_h^* \rangle \end{bmatrix} \tag{1}$$

where T_α is the brightness temperature for component α, λ the wavelength, k_B Boltzmann's constant, η impedance of the medium, and E_α the electric field for polarization α. The subscript α is equal to v, h, 3, and 4 when referring, respectively, to the first, second, third, and fourth Stokes parameters, and it equals 45, -45, cl, and cr for $+45^\circ$ linear, -45° linear, left-handed circularly, and right-handed circularly polarized brightness temperatures, respectively. The two equivalent definitions of the third and fourth Stokes parameter in (1) have stimulated the development of two fundamentally distinct polarimetric radiometer architectures, i.e., that of a correlating polarimeter [4] and an adding polarimeter [3]. Correlation of two orthogonal wave amplitudes can furthermore be performed using either analog [7] or digital detection hardware [8]. The adding polarimeter (e.g., see [9] and [10]) requires the incoherent detection of at least four orthogonal mode combinations along with postdetection differencing.

Manuscript received August 26, 2001; revised October 17, 2002. This work was supported in part by the National Technology Agency of Finland (Tekes) under Contract 40206/98, the Graduate School in Electronics, Telecommunication and Automation (GETA), the Foundation of Technology, the Vilho, Yrjö and Kalle Väisälä Foundation, the U.S. National Polar Orbiting Environmental Satellite System Integrated Program Office, and by the National Aeronautics and Space Administration under Grant NAGW-4191.

J. Lahtinen was with the Laboratory of Space Technology, Helsinki University of Technology, 02015 HUT, Finland. He is now with the European Space Agency, ESTEC, TOS-ETP, 2200 AG Noordwijk ZH, The Netherlands (e-mail: janne.lahtinen@esa.int).

A. J. Gasiewski is with the National Oceanic and Atmospheric Administration, Environmental Technology Laboratory, Boulder, CO 80305-3328 USA (e-mail: al.gasiewski@noaa.gov).

M. Klein is with the University of Colorado, Cooperative Institute for Research in Environmental Science (CIRES), Boulder, CO 80305-3328 USA (e-mail: marian.klein@noaa.gov).

I. Corbella is with the Department of Signal Theory and Communications, Universitat Politècnica de Catalunya, E.T.S.E. Telecomunicatió, 08071 Barcelona, Spain (e-mail: corbella@tsc.upc.es).

Digital Object Identifier 10.1109/TGRS.2003.810203

Despite extensive work in passive polarimetric applications, relatively little has been published on the calibration of polarimetric radiometers, with the publication by Gasiewski and Kunkee [11] (hereafter referred to as the GK technique) being the seminal work in this area. In the GK study a practical means was proposed for accurately calibrating a tripolarimetric (i.e., first three Stokes parameters) radiometer from its antenna through its analog-to-digital converters using relatively simple hardware. However, the study did not address the calibration of the fourth Stokes parameter. Accordingly, we have extended the GK technique for end-to-end calibration of a fully polarimetric radiometer using a similar simple passive standard. The standard is based on that described in [11], i.e., being composed of two blackbodies of different but precisely known emission temperatures along with a polarization-splitting wire-grid. In order to generate a precisely known set of T_4 values, we incorporate further a microwave phase retardation plate. We discuss herein the general requirements for fully polarimetric calibration using this system, along with an error analysis, and demonstrate a fully polarimetric calibration standard for laboratory usage. The feasibility of the calibration method and constraints on such a standard suitable for wind vector polarimetry are also discussed.

II. Theoretical Background

A. General Requirements for Fully Polarimetric Calibration

A well-designed single-polarization radiometer is highly linear in its response to antenna temperature, thus warranting a two-blackbody technique for calibration (e.g., see [12]). In the two-blackbody technique one needs to identify only two unknown system parameters (the gain and offset) using two distinct but precisely known antenna temperatures. The radiometer's response to the third and fourth Stokes parameters as well as cross-polarization leakage is generally neglected in single and dual polarization systems, and justifiably so, provided that the blackbody standards are themselves unpolarized. Both analog and digital radiometers [13] can be calibrated in this manner.

A fully polarimetric radiometer, in contrast, will generally exhibit some sensitivity in each channel to all four Stokes parameters, and thus requires more than two distinct input stimuli for complete calibration. Based on the formulation for a tripolarimetric radiometer [11] the complete output response of a fully polarimetric radiometer can be written as

$$\begin{aligned}\overline{r} &= \begin{bmatrix} r_v \\ r_h \\ r_3 \\ r_4 \end{bmatrix} \\ &= \begin{bmatrix} g_{vv} & g_{vh} & g_{v3} & g_{v4} \\ g_{hv} & g_{hh} & g_{h3} & g_{h4} \\ g_{3v} & g_{3h} & g_{33} & g_{34} \\ g_{4v} & g_{4h} & g_{43} & g_{44} \end{bmatrix} \begin{bmatrix} T_v \\ T_h \\ T_3 \\ T_4 \end{bmatrix} + \begin{bmatrix} o_v \\ o_h \\ o_3 \\ o_4 \end{bmatrix} + \overline{n} \\ &= \overline{\overline{g}}\overline{T}_B + \overline{o} + \overline{n} \end{aligned} \tag{2}$$

where $\overline{r}$ is video output response vector; $\overline{\overline{g}}$ and $\overline{o}$ consist of radiometer gain and offset parameters; and $\overline{n}$ is the instrument noise referred to the video outputs. The off-diagonal elements of $\overline{\overline{g}}$ represent interchannel crosstalk, which can be the result of one or more hardware limitations, including a) limited polarization isolation in the antenna, b) cross-talk in the video or microwave circuitry, c) unbalance or cross-talk in the correlator, depending on the correlator type and configuration, and d) phase imbalances in the predetected signals used to measure T_3 or T_4. In order to invert the antenna brightness temperature vector from $\overline{r}$, the elements of $\overline{\overline{g}}$ and $\overline{o}$ in (2) are required. Owing to instrument drift, their determination generally needs to be performed periodically, with the period determined by the gain and offset autocorrelation rolloff characteristics (e.g., see [14]).

During calibration, a variety of reference brightness vectors $\overline{T}_{Bi}$ are presented to the antenna, resulting in the acquisition of a calibration data matrix $\overline{\overline{C}}$

$$\overline{\overline{C}} = \begin{bmatrix} \overline{T}_{B1}^T & 1 \\ \overline{T}_{B2}^T & 1 \\ \cdots & \cdots \\ \overline{T}_{BM}^T & 1 \end{bmatrix} \tag{3}$$

where M is the number of distinct observations, or calibration "looks." We represent the relationship between the radiometer response for one channel and the calibration data matrix by:

$$\begin{aligned}\begin{pmatrix} r_{C\alpha}(1) \\ r_{C\alpha}(2) \\ \cdots \\ r_{C\alpha}(M) \end{pmatrix} &= [\overline{T}_{Cv} \quad \overline{T}_{Ch} \quad \overline{T}_{C3} \quad \overline{T}_{C4} \quad \overline{1}] \cdot \begin{pmatrix} g_{\alpha v} \\ g_{\alpha h} \\ g_{\alpha 3} \\ g_{\alpha 4} \\ o_\alpha \end{pmatrix} \\ &= \overline{\overline{C}} \cdot \begin{bmatrix} \overline{g}_\alpha \\ o_\alpha \end{bmatrix} \end{aligned} \tag{4}$$

where $\overline{1}$ is a unity vector of length M; the subscript α can be either v, h, 3, or 4. In order to determine the elements in the gain matrix and offset vector the set of calibration looks must fulfill two requirements: a) the reference brightness vectors must be able to be determined *a priori* with adequate precision and timeliness, and b) the number of linearly independent brightness vectors must be greater than or equal to the number of gain/offset unknowns for each channel, i.e., $\overline{\overline{C}}$ must be full rank. For the fully polarimetric case the minimum rank is five, unless one or more of the unknown gain/offsets parameters can be predetermined and held fixed by careful design and stabilization.

B. Passive Polarimetric Calibration Hardware

Using the GK polarized standard [11] (heretofore referred to as a "linearly polarized standard"), a maximum of three linearly independent Stokes vectors along with an unpolarized Stokes vector can be generated. The unpolarized vector is obtained, e.g., by removing the polarizing wire grid. This set of vectors facilitates calibration of the first three Stokes channels. In order to calibrate the fourth Stokes channel, a precision circularly polarized signal can be generated by inserting a biaxial phase retardation plate between the linearly polarized standard and the radiometer antenna. The retardation plate generates a predetermined phase shift between the perpendicular field components of the transmitted waves. We refer to this combination of a linearly polarized standard and a retardation plate as a "fully polarimetric standard" (Fig. 1).

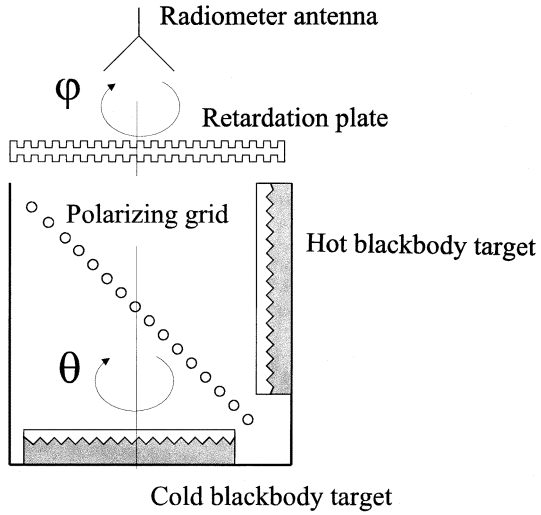

Fig. 1. Schematic diagram of the NOAA/ETL fully polarimetric calibration standard.

The *a priori* determination of the Stokes vector generated by such a standard proceeds by first calculating the tripolarimetric Stokes vector of the linearly polarized standard, then multiplying this vector by a transformation matrix describing the influence of the retardation plate. The tripolarimetric Stokes vector $\overline{T}_T$ is [11]

$$\begin{aligned}\overline{T}_T &= \begin{bmatrix} T_v \\ T_h \\ T_3 \\ T_4 \end{bmatrix} \\ &= \begin{bmatrix} \cos^2\theta & \sin^2\theta \\ \sin^2\theta & \cos^2\theta \\ \sin(2\theta) & -\sin(2\theta) \\ 0 & 0 \end{bmatrix} \cdot \begin{bmatrix} T'_{\mathrm{HOT}} \\ T'_{\mathrm{COLD}} \end{bmatrix} \qquad (5) \\ &= \overline{\overline{G}} \cdot \begin{bmatrix} T'_{\mathrm{HOT}} \\ T'_{\mathrm{COLD}} \end{bmatrix} \\ \begin{bmatrix} T'_{\mathrm{HOT}} \\ T'_{\mathrm{COLD}} \end{bmatrix} &= \begin{bmatrix} r_{\|} & t_{\|} & L_{\|} \\ r_{\perp} & t_{\perp} & L_{\perp} \end{bmatrix} \cdot \begin{bmatrix} T_{\mathrm{HOT}} \\ T_{\mathrm{COLD}} \\ T_G \end{bmatrix} \\ &= \overline{\overline{A}} \cdot \begin{bmatrix} T_{\mathrm{HOT}} \\ T_{\mathrm{COLD}} \\ T_G \end{bmatrix} \qquad (6)\end{aligned}$$

where T_{HOT} and T_{COLD} are the hot and cold blackbody brightness temperatures, respectively; T_G is the physical temperature of the polarizing grid; and $r_{\|}$, $t_{\|}$, and $L_{\|}$ are reflection coefficient, transmission coefficient, and ohmic losses of the grid for the waves polarized parallel to grid wires, respectively. The analogous parameters for waves polarized perpendicular to the grid wires are $r_{\perp}$, $t_{\perp}$, and $L_{\perp}$, respectively. The losses of the polarizing grid are assumed to be included as in [15]. The grid wire orientation angle measured with respect to the antenna polarization basis is θ, with $\theta = 0^{\circ}$ defined by the grid wires being aligned parallel to the radiometer's vertical polarization axis. We assume that $L_{\perp} = (1 - r_{\perp} - t_{\perp})$ and $L_{\|} = \left(1 - r_{\|} - t_{\|}\right)$, which is the case for grids with close and uniform wire spacing.

To simplify our analysis, we first ignore the thermal emission contribution from the retardation plate. Using (5) and (6), the Stokes vector generated upon insertion of the retardation plate is

$$\overline{T}'_C = \overline{\overline{F}}^T \cdot \overline{T}_T = \overline{\overline{F}}^T \cdot \overline{\overline{G}} \cdot \overline{\overline{A}} \cdot \begin{bmatrix} T_{\mathrm{HOT}} \\ T_{\mathrm{COLD}} \\ T_G \end{bmatrix} \qquad (7)$$

$$\overline{\overline{F}} = [\overline{F}_v \quad \overline{F}_h \quad \overline{F}_3 \quad \overline{F}_4] \qquad (8)$$

$$\begin{aligned}\overline{F}_{\alpha} &= \begin{bmatrix} D_{\alpha 11} & D_{\alpha 12} & D_{\alpha 13} & D_{\alpha 14} & D_{\alpha 15} \\ D_{\alpha 21} & D_{\alpha 22} & D_{\alpha 23} & D_{\alpha 24} & D_{\alpha 25} \\ D_{\alpha 31} & D_{\alpha 32} & D_{\alpha 33} & D_{\alpha 34} & D_{\alpha 35} \\ D_{\alpha 41} & D_{\alpha 42} & D_{\alpha 43} & D_{\alpha 44} & D_{\alpha 45} \end{bmatrix} \begin{bmatrix} 1 \\ \cos(2\varphi) \\ \cos(4\varphi) \\ \sin(2\varphi) \\ \sin(4\varphi) \end{bmatrix} \\ &= \overline{\overline{D}}_{\alpha} \cdot \begin{bmatrix} 1 \\ \cos(2\varphi) \\ \cos(4\varphi) \\ \sin(2\varphi) \\ \sin(4\varphi) \end{bmatrix} \qquad (9)\end{aligned}$$

where φ is the rotation angle of the plate relative to the radiometer. Here, $\varphi = 0^{\circ}$ refers to the case where the retardation plate's slow axis is parallel to the radiometer antenna's vertical polarization. The nonzero elements of $\overline{\overline{D}}_{\alpha}$ are

$$D_{v11} = D_{h21} = \frac{3}{8}\left(\frac{1}{l_{\|}^2} + \frac{1}{l_{\perp}^2}\right) + \frac{1}{4}\frac{\cos(\zeta)}{l_{\|} l_{\perp}} \qquad (10)$$

$$\begin{aligned}D_{v12} &= 2D_{v34} = -D_{h22} = 2D_{h34} = D_{314} = D_{324} \\ &= \frac{1}{2}\left(\frac{1}{l_{\|}^2} - \frac{1}{l_{\perp}^2}\right) \qquad (11)\end{aligned}$$

$$D_{v21} = D_{h11} = \frac{1}{8}\left(\frac{1}{l_{\|}^2} + \frac{1}{l_{\perp}^2}\right) - \frac{1}{4}\frac{\cos(\zeta)}{l_{\|} l_{\perp}} \qquad (12)$$

$$\begin{aligned}2D_{v13} &= -2D_{v23} = 2D_{v35} = -2D_{h13} \\ &= 2D_{h23} = -2D_{h35} = -D_{333} = D_{315} \\ &= -D_{325} = \frac{1}{4}\left[\frac{1}{l_{\|}^2} + \frac{1}{l_{\perp}^2} - 2\frac{\cos(\zeta)}{l_{\|} l_{\perp}}\right] \qquad (13)\end{aligned}$$

$$\begin{aligned}2D_{v44} &= -2D_{h44} = -D_{342} \\ &= D_{432} = -D_{414} = D_{424} = \frac{\sin(\zeta)}{l_{\|} l_{\perp}} \qquad (14)\end{aligned}$$

$$D_{331} = \frac{1}{4}\left[\frac{1}{l_{\|}^2} + \frac{1}{l_{\perp}^2} + 2\frac{\cos(\zeta)}{l_{\|} l_{\perp}}\right] \qquad (15)$$

$$D_{441} = \frac{\cos(\zeta)}{l_{\perp} l_{\|}} \qquad (16)$$

where $\zeta = k_{\|} \cdot d - k_{\perp} \cdot d$ is the relative phase shift between the slow and fast axes of the plate; d is the plate thickness; and $k_{\|}$ and $k_{\perp}$ are wave numbers for electric fields parallel and perpendicular to the slow axis of the retardation plate, respectively.

The losses of the retardation plate in the slow and fast axes are

$$l_s = e^{\alpha_s \cdot d} \qquad (17)$$

where α_s is the (nonnegative) power attenuation coefficient of the plate for the electric field parallel $(s = \|)$ and perpendicular

TABLE I
AN EXAMPLE OF A FULLY POLARIMETRIC CALIBRATION SEQUENCE ALONG WITH THE CORRESPONDING *A PRIORI* BRIGHTNESS VECTORS GENERATED FOR AN IDEAL STANDARD

Calibration target parameters		Generated brightness temperature			
θ	φ	T_v	T_h	T_3	T_4
0°	0°	T_{HOT}	T_{COLD}	0	0
90°	0°	T_{COLD}	T_{HOT}	0	0
45°	0°	$(T_{HOT}+T_{COLD})/2$	$(T_{HOT}+T_{COLD})/2$	$(T_{HOT}-T_{COLD})\cdot\cos(\zeta)$	$(T_{HOT}-T_{COLD})\cdot\sin(\zeta)$
45°	90°	$(T_{HOT}+T_{COLD})/2$	$(T_{HOT}+T_{COLD})/2$	$(T_{HOT}-T_{COLD})\cdot\cos(\zeta)$	$(T_{COLD}-T_{HOT})\cdot\sin(\zeta)$
Unpolarized target		T_{UP}	T_{UP}	0	0

$(s = \perp)$ to the slow axis (respectively). The attenuation coefficient is obtained by [16]

$$\alpha_s = -\mathrm{Im}\left\{2\pi f\sqrt{\mu_s\left(\varepsilon_s' - j\varepsilon_s''\right)}\right\} \tag{17}$$

where f is frequency, and μ_s and $\varepsilon_s' - j\varepsilon''$ are the effective permeability and complex dielectric constant of the retardation plate, respectively. The derivation of (10)–(16) for vertical polarization has been presented earlier in [17] for the lossless case. For the general (lossy) case, we present the results for all four Stokes parameters in Appendix A, with the detailed derivation available in [18].

Various retardation plate designs have been presented in [19]. A practical retardation plate is a slab of dielectric material with parallel grooves machined on one or both sides (configuration "D" in [19]). Suitable materials include, e.g., polytetrafluoroethylene (PTFE, also known by its trade name as Teflon), polyethylene, or cross-linked polystyrene (known by its trade name as Rexolite). The effective dielectric constant of a grooved plate is different along the axes parallel (slow axis) and perpendicular (fast axis) to the grooves. To determine the dielectric constants the machined grooves of the retardation plate and ridges between them can be considered to be capacitors filled with air and dielectric, respectively. For the electric field parallel to the grooves the capacitors behave as if connected in parallel; for the electric field perpendicular to the grooves the capacitors behave as if connected in series. The effective complex dielectric constants for fields both parallel and perpendicular to the grooves are thus approximately [17]

$$\varepsilon_{\|} = p\varepsilon_1 + (1-p)\varepsilon_2 \tag{19}$$

$$\varepsilon_{\perp} = \frac{\varepsilon_1\varepsilon_2}{p\varepsilon_2 + (1-p)\varepsilon_1} \tag{20}$$

where the subscripts "1" and "2" refer to the bulk dielectric material and the surrounding medium (e.g., air), respectively. The symbol p stands for the fill factor of the plate, i.e., the relative thickness of material between the grooves.

Expressions for groove depths and fill factors for given phase shifts are provided in [20] and [21]. In practice, the plate's solid and grooved layers are optimized in thickness to minimize reflections and preclude grating lobes. Good estimates for the losses $l_{\|}$ and $l_{\perp}$ are the products of the individual losses of the grooved and solid layers of the slab. However, this approach does not include the secondary effects of internal reflection or diffraction (e.g., see [22]), which remain to be studied.

Upon inclusion of the brightness temperature contribution of the retardation plate $\overline{T}_R$ the resulting fully polarimetric Stokes vector $\overline{T}_C$ becomes

$$\overline{T}_C = \overline{T}_C' + \overline{T}_R \tag{21}$$

$$\overline{T}_R = \frac{T_{P,R}}{2}\begin{bmatrix} 2 - \frac{1}{l_{\|}^2} - \frac{1}{l_{\perp}^2} + \left(\frac{1}{l_{\perp}^2} - \frac{1}{l_{\|}^2}\right)\cos(2\varphi) \\ 2 - \frac{1}{l_{\|}^2} - \frac{1}{l_{\perp}^2} + \left(\frac{1}{l_{\|}^2} - \frac{1}{l_{\perp}^2}\right)\cos(2\varphi) \\ 2\left(\frac{1}{l_{\perp}^2} - \frac{1}{l_{\|}^2}\right)\sin(2\varphi) \\ 0 \end{bmatrix} \tag{22}$$

where $T_{P,R}$ is the physical temperature of the retardation plate. (The derivation of (22) is presented in [18].) The fully polarimetric standard, along with an unpolarized blackbody (realized, for example, by removing both the retardation plate and grid) can be used to generate four linearly independent polarized Stokes vectors along with an unpolarized Stokes vector. Collectively, this set of Stokes vectors facilitates precise calibration of all four Stokes parameters provided that the various material and component parameters of the standard are adequately known.

Changing θ and φ can provide an infinite number of distinct calibration data matrix rows. As a practical example, one particularly useful and complete set of reference Stokes vectors is described in Table I. Note that in order to avoid the removal of the retardation plate during the calibration process the generation of mixed linearly and circularly polarized signals is required. Thus, the phase shift of the retardation plate should be significantly different from 90° or its multiples.

C. Calibration Matrix Inversion and Uncertainties

By rotating the linearly polarized standard and the retardation plate over a range of angles θ and φ, respectively, along with applying unpolarized looks, a full-rank set of Stokes vectors can be observed

$$\overline{\overline{T}}_C = \begin{bmatrix} \overline{T}_{Cv,0}^T \\ \overline{T}_{Ch,0}^T \\ \overline{T}_{C3,0}^T \\ \overline{T}_{C4,0}^T \end{bmatrix} + \begin{bmatrix} \Delta\overline{T}_{Cv}^T \\ \Delta\overline{T}_{Ch}^T \\ \Delta\overline{T}_{C3}^T \\ \Delta\overline{T}_{C4}^T \end{bmatrix} = \overline{\overline{T}}_{C,0} + \Delta\overline{\overline{T}}_C \tag{23}$$

where $\overline{\overline{T}}_{C,0}$ represents the generated *a priori* Stokes vector set, and $\Delta\overline{\overline{T}}_C$ is a matrix of uncertainties in the calibration looks

caused by imperfect knowledge of the parameters of various components. The elements of $\Delta\overline{T}_{C\alpha}$ are

$$\Delta T_{C\alpha,i} = \sqrt{\sum_{j=1}^{N} s_{\alpha,ij}^2 \sigma_{pj}^2} \tag{24}$$

where the subscript i stands for one of M configurations of the calibration standard. The standard deviations of each component parameter, σ_{pj}, are the rms parameter errors, $\left(\langle \delta_{pj}^2 \rangle\right)^{1/2}$, presumed calculable over an ensemble of similar components. The $s_{\alpha,ij}$ are elements of a Jacobian relating small variations in these parameters to elements of the Stokes vector

$$s_{\alpha,ij} = \left| \frac{\partial T_{C\alpha,0,i}}{\partial \delta_{pj}} \right|. \tag{25}$$

The subscript j is a parameter index that ranges from 1 to the number of parameters N.

The parameter errors can be further partitioned into either systematic or random uncertainties. Systematic uncertainties are time invariant and do not change between calibrations. These uncertainties include, for example, most of the uncertainties of the polarizing grid and retardation plate, as well as beam spillover and effects of radiometer passband averaging. Random uncertainties include physical temperature errors, grid or plate degradations, and the possible effects of variable amounts of moisture condensation, background brightness, and beam misalignment (if present). Since error in the calibrated brightness temperatures due to systematic uncertainties can be compensated for *a posteriori* (at least in part), we consider these two classes of uncertainties separately. Indeed, an improved determination of calibration standard characteristics (e.g., retardation plate phase shift) and/or calibration using data observed using other independent standards can be used to reduce systematic errors.

The parameter uncertainty vectors for major random, systematic, and total uncertainties can thus be defined as

$$\begin{aligned}\overline{\delta}_p = \overline{\delta}_R + \overline{\delta}_S &= \begin{bmatrix} \delta_{R1} \\ \delta_{R2} \\ \cdots \\ \delta_{RN} \end{bmatrix} + \begin{bmatrix} \delta_{S1} \\ \delta_{S2} \\ \cdots \\ \delta_{SN} \end{bmatrix} \\ &= \begin{bmatrix} \delta_{R,T_{P,\mathrm{HOT}}} \\ \delta_{R,T_{P,\mathrm{COLD}}} \\ 0 \\ 0 \\ 0 \\ 0 \\ \delta_{R,T_G} \\ \delta_{R,\theta} \\ 0 \\ \\ \delta_{R,\varphi} \\ 0 \\ 0 \\ 0 \\ \delta_{R,T_{P,R}} \\ \\ \delta_{R,T_{P,\mathrm{UP}}} \end{bmatrix} + \begin{bmatrix} \delta_{S,T_{P,\mathrm{HOT}}} \\ \delta_{S,T_{P,\mathrm{COLD}}} \\ \delta_e \\ \delta_{t_\parallel} \\ \delta_{r_\parallel} \\ \delta_{L_\parallel} \\ \delta_{S,T_G} \\ \delta_{S,\theta} \\ \delta_\phi \\ \\ \delta_{S,\varphi} \\ \delta_\zeta \\ \delta_{l_\parallel} \\ \delta_{l_\perp} \\ \delta_{S,T_{P,R}} \\ \\ \delta_{S,T_{P,\mathrm{UP}}} \end{bmatrix} \end{aligned} \tag{26}$$

where the subscripts R and S refer to random and systematic uncertainties, respectively. For simplicity, it is assumed that $t_\parallel = r_\perp$, $r_\parallel = t_\perp$, and $L_\parallel = L_\perp$ in the above. The uncertainties of the linearly polarized standard are characterized by the uncertainties of the hot and cold (or ambient) blackbody physical temperatures, their emissivities, the transmissivity, reflectivity, ohmic losses and physical temperature of the polarizing grid, rotation angle, and the phase shift between the vertical and horizontal brightness temperatures (described by $\delta_{T_{P,\mathrm{HOT}}}$, $\delta_{T_{P,\mathrm{COLD}}}$, δ_e, $\delta_{t_\parallel}\delta_{r_\parallel}\delta_{L_\parallel}\delta_{T_G}$, δ_θ, and δ_ϕ, respectively). The uncertainties of the retardation plate are characterized by the uncertainty of rotation angle, phase shift, losses parallel and perpendicular to the plate slow axis, and physical temperature (described by δ_φ, δ_ζ, $\delta_{l_\parallel}$, $\delta_{l_\perp}$, and $\delta_{T_{P,R}}$, respectively). It is assumed that a separate unpolarized blackbody is also used, for which the uncertainty of its physical temperature is $\delta_{T_{P,\mathrm{UP}}}$. This variable is redundant with $\delta_{T_{P,\mathrm{HOT}}}$ or $\delta_{T_{P,\mathrm{COLD}}}$ if either the hot or cold blackbody of the linearly polarized standard is used as an unpolarized target. In (26), we have assumed that all blackbodies have identical emissivities, although this assumption is not necessary.

During calibration the response of a single radiometer channel is

$$\overline{r}_{C\alpha} = \begin{bmatrix} \overline{\overline{T}}_{C,0}^T & \overline{1} \end{bmatrix} \begin{bmatrix} g_{\alpha v} \\ g_{\alpha h} \\ g_{\alpha 3} \\ g_{\alpha 4} \\ o_\alpha \end{bmatrix} + \Delta\overline{\overline{T}}_C^T \begin{bmatrix} \langle g_{\alpha v} \rangle \\ \langle g_{\alpha h} \rangle \\ \langle g_{\alpha 3} \rangle \\ \langle g_{\alpha 4} \rangle \end{bmatrix} + \overline{n}_\alpha. \tag{27}$$

Similarly, the fully polarimetric response is

$$\overline{\overline{r}}_C = \overline{\overline{C}}_0 \left[\overline{\overline{g}} \quad \overline{o}\right]^T + \Delta\overline{\overline{T}}_C^T \left\langle \overline{\overline{g}} \right\rangle^T + \overline{\overline{n}} = \overline{\overline{C}}_0 \left[\overline{\overline{g}} \quad \overline{o}\right]^T + \overline{\overline{n}}_T \tag{28}$$

where $\overline{\overline{C}}_0$ is the Stokes vector matrix (augmented with a unity column vector), and $\left[\overline{\overline{g}} \;\; \overline{o}\right]^T$ is the unknown gain-offset matrix. The total uncertainty $\overline{\overline{n}}_T$ consists of the sum of both radiometric integration noise $\overline{\overline{n}}$ and the random errors of the calibration standard. Long integration times can be used to reduce $\overline{\overline{n}}$, which falls as the inverse square root of the integration time, but only insofar as system drift errors remain small.

The estimation of the gain-offset estimate matrix is straightforward in the case where the inverse of $\overline{\overline{C}}_0$ exists

$$\left[\overline{\hat{\overline{g}}} \quad \overline{\hat{o}}\right]^T = \overline{\overline{C}}_0^{-1} \overline{\overline{r}}_C. \tag{29}$$

In order to reduce calibration uncertainties, however, it is desirable to have an overdetermined C_0 matrix, i.e., to include more than five independent observations. In this case, estimates for the unknown gain and offset parameters can be found by pseudoinversion [11], [23]

$$\left[\overline{\hat{\overline{g}}} \quad \overline{\hat{o}}\right]^T = \left(\overline{\overline{C}}_0^T \overline{\overline{C}}_0\right)^{-1} \overline{\overline{C}}_0^T \overline{\overline{r}}_C. \tag{30}$$

The above inverse is guaranteed to exist provided that a full rank set of Stokes observations are made and that the uncertainty $\overline{\overline{n}}_T$ is small enough. Splitting the gain-offset estimate matrix into

separate $\overline{\overline{\hat{g}}}$ and $\overline{\hat{o}}$, the scene brightness temperatures are subsequently computed from the radiometer responses by

$$\overline{\overline{T}}_B^T = \overline{\overline{T}}_{B,0}^T + \Delta\overline{\overline{T}}_B^T = \left(\overline{\overline{r}}_B - \overline{1}\,\overline{\hat{o}}^T\right)\left(\overline{\overline{\hat{g}}}^T\right)^{-1} \tag{31}$$

$$\overline{\overline{T}}_{B,0} = \left[\overline{T}_{v,0} \quad \overline{T}_{h,0} \quad \overline{T}_{3,0} \quad \overline{T}_{4,0}\right]^T \tag{32}$$

where $\overline{\overline{T}}_{B,0}$, $\Delta\overline{\overline{T}}_B$, and $\overline{\overline{r}}_B$ represent the Stokes vector for the scene, uncertainties in the measured brightness temperatures, and radiometer responses, respectively. The length of the unity column vector $\overline{1}$ corresponds to the number of the scenes. It is assumed in the above approach that the gain-offset matrix elements are statistically independent and that no *a priori* information is used in their determination. If correlations between any of the elements of $[\overline{\overline{g}} \quad \overline{o}]^T$ exist in between calibrations (e.g., due to internal radiometer temperature drift), then these correlations could potentially be utilized beneficially within a statistical (rather than pseudo-) inversion.

It is noted that the phase shift of a retardation plate increases approximately linearly with frequency over nonzero radiometric bandwidths. However, the *a priori* brightness temperatures of the third and fourth Stokes parameters are functions of $\cos(\zeta)$ and $\sin(\zeta)$, respectively, and are not linear. The resulting nonlinearity can lead to small errors in determining the *a priori* brightness temperatures over the entire bandwidth of a radiometer unless a suitable set of calculated Stokes vectors is averaged over the radiometer band. These errors, however, are of second order. Assuming, for example, a 400-MHz wide band centered at 18.7 GHz and a calibration standard with 200-K hot–cold temperature difference, we calculate that the errors remain below 0.01 and 0.04 K for third and fourth Stokes parameters for phase shifts up 90° and 180°, respectively. Note, however, that the third and fourth Stokes parameters diminish for phase shift values near 90° and 0°, respectively, leading to higher calibration errors near these cardinal values. For reasons of both accuracy and convenience, it is thus desirable to fabricate the retardation plate to be near $\lambda/8$ in differential phase delay.

Among other potential sources of error are thermal variations in the dimensions of the retardation plate and target asymmetries. However, the same number of polarizing molecules is present during thermal expansion; hence, phase shifts along the principal axes remain fairly constant with temperature. Use of symmetry in the fabrication of the linearly polarized target, retardation plate, and associated rotation hardware insures against polarization basis skew and polarization crosstalk. Errors resulting from asymmetry can generally be associated with errors in rotation angle and phase shift and can be analyzed as such.

D. Accuracy and Sensitivity Issues

The uncertainties in the calibration standard parameters have a significant impact on the overall absolute accuracy of the calibrated radiometer. The impact of these uncertainties can be modeled as small deviations from the true gain-offset matrix, *viz*,

$$\left[\overline{\overline{\hat{g}}} \quad \overline{\hat{o}}\right]^T = \left[\overline{\overline{g}} \quad \overline{o}\right]^T + \left[\overline{\overline{\delta g}} \quad \overline{\delta o}\right]^T. \tag{33}$$

Similar to (30), the gain-offset uncertainty matrix is related to calibration noise by

$$\left[\overline{\overline{\delta g}} \quad \overline{\delta o}\right]^T = \left(\overline{\overline{C}}_0^T\overline{\overline{C}}_0\right)^{-1}\overline{\overline{C}}_0^T\overline{\overline{n}}_T. \tag{34}$$

Assuming that the radiometer has a sufficiently long integration time during calibration, the integration noise can be made negligible compared to calibration standard uncertainties, in which case

$$\left[\overline{\overline{\delta g}} \quad \overline{\delta o}\right]^T \approx \left(\overline{\overline{C}}_0^T\overline{\overline{C}}_0\right)^{-1}\overline{\overline{C}}_0^T\Delta\overline{\overline{T}}_C^T\overline{\overline{\hat{g}}}^T. \tag{35}$$

The corresponding uncertainty in the scene Stokes vector as a result of the gain-offset uncertainty can be obtained using $r_B = C_{B,0}\left[\overline{\overline{g}} \quad \overline{o}\right]^T$ and (31), (33), and (35)

$$\begin{aligned}\Delta\overline{\overline{T}}_B^T &= -\overline{\overline{C}}_{B,0}\left[\overline{\overline{\delta g}} \quad \overline{\delta o}\right]^T\left(\overline{\overline{\hat{g}}}^T\right)^{-1}\\ &\approx -\overline{\overline{C}}_{B,0}\left(\overline{\overline{C}}_0^T\overline{\overline{C}}_0\right)^{-1}\overline{\overline{C}}_0^T\Delta\overline{\overline{T}}_C^T\end{aligned} \tag{36}$$

where $\overline{\overline{C}}_{B,0}$ is the scene brightness matrix acquired during operation, augmented with a unity column vector as follows:

$$\overline{\overline{C}}_{B,0} = \left[\overline{\overline{T}}_{B,0}^T \quad \overline{1}\right]. \tag{37}$$

The elements of the gain-offset uncertainty matrix exhibit interdependencies that can be examined using a gain-offset error covariance matrix

$$\begin{aligned}\overline{\overline{R}}_{\left[\overline{\overline{\delta g}} \quad \overline{\delta o}\right]^T} &= \left\langle\left[\overline{\overline{\delta g}} \quad \overline{\delta o}\right]^T\left[\overline{\overline{\delta g}} \quad \overline{\delta o}\right]\right\rangle\\ &= \left(\overline{\overline{C}}_0^T\overline{\overline{C}}_0\right)^{-1}\overline{\overline{C}}_0^T\underbrace{\left\langle\overline{\overline{n}}_T\overline{\overline{n}}_T^T\right\rangle}_{\overline{\overline{R}}_{\overline{\overline{n}}_T}}\overline{\overline{C}}_0\left(\overline{\overline{C}}_0^T\overline{\overline{C}}_0\right)^{-1}.\end{aligned} \tag{38}$$

Since the integration noise and calibration standard errors are uncorrelated, the total calibration error covariance matrix is

$$\overline{\overline{R}}_{\overline{\overline{n}}_T} = \overline{\overline{R}}_{\overline{\overline{n}}} + \overline{\overline{R}}_{\Delta\overline{\overline{T}}_C^T\overline{\overline{\hat{g}}}^T}. \tag{39}$$

Applying sufficiently long integration times removes the integration noise component, leaving

$$\begin{aligned}\overline{\overline{R}}_{\overline{\overline{n}}_T} &\approx \overline{\overline{R}}_{\Delta\overline{\overline{T}}_C^T\overline{\overline{\hat{g}}}^T} = \left\langle\Delta\overline{\overline{T}}_C^T\overline{\overline{\hat{g}}}^T\overline{\overline{\hat{g}}}\Delta\overline{\overline{T}}_C\right\rangle\\ &= \begin{bmatrix} R_{11} & \cdots & R_{1M}\\ \cdots & \ddots & \cdots\\ R_{M1} & \cdots & R_{MM}\end{bmatrix}\end{aligned} \tag{40}$$

$$\begin{aligned}R_{ab} = \sum_{\alpha=v}^{4}\sqrt{\sum_{j=1}^{N}\left\langle s_{\alpha,aj}^2 s_{\alpha,bj}^2\right\rangle\sigma_{pj}^4}\\ \cdot\left(\langle g_{v\alpha}\rangle^2 + \langle g_{h\alpha}\rangle^2 + \langle g_{3\alpha}\rangle^2 + \langle g_{4\alpha}\rangle^2\right).\end{aligned} \tag{41}$$

The covariance matrix of the scene Stokes vector errors now becomes

$$\overline{\overline{R}}_{\Delta\overline{\overline{T}}_B^T} \approx \overline{\overline{C}}_{B,0}\left(\overline{\overline{C}}_0^T\overline{\overline{C}}_0\right)^{-1}\overline{\overline{C}}_0^T\underbrace{\left\langle\Delta\overline{\overline{T}}_C^T\Delta\overline{\overline{T}}_C\right\rangle}_{\overline{\overline{R}}_{\Delta\overline{\overline{T}}_C^T}}\overline{\overline{C}}_0 \cdot\left(\overline{\overline{C}}_0^T\overline{\overline{C}}_0\right)^{-1}\overline{\overline{C}}_{B,0}^T \tag{42}$$

$$\overline{\overline{R}}_{\Delta\overline{\overline{T}}_C^T} = \begin{bmatrix} P_{11} & \cdots & P_{1M} \\ \cdots & \ddots & \cdots \\ P_{M1} & \cdots & P_{MM} \end{bmatrix} \tag{43}$$

$$P_{ab} = \sum_{\alpha=v}^{4}\sqrt{\sum_{j=1}^{N}\left\langle s_{\alpha,aj}^2 s_{\alpha,bj}^2\right\rangle\sigma_{pj}^4}. \tag{44}$$

Equations (42)–(44) relate the correlated error covariances associated with the use of the standard to the associated errors in the scene Stokes vectors, and provide a means of determining the overall impact on radiometric accuracy.

III. Laboratory Demostration of Fully Polarimetric Calibration

To demonstrate fully polarimetric calibration an experiment was carried out in June 1999 at the facilities of the U.S. National Oceanic and Atmospheric Administration's (NOAA) Environmental Technology Laboratory (ETL) in Boulder, CO. The fully polarimetric 10.7-GHz receiver of NOAA/ETL Polarimetric Scanning Radiometer (PSR) [13] was used for this study. An existing linearly polarized calibration standard was upgraded into a fully polarimetric calibration standard by the addition of a $\sim\lambda/8$ phase retardation plate. (A similar fully polarimetric standard was developed also at the Helsinki University of Technology, Laboratory of Space Technology [21], [24].)

A. Radiometric Equipment

The NOAA PSR is an airborne multifrequency polarimetric imaging radiometer with total power receivers at 10.7, 18.7, 21.45, 37, and 89 GHz.[1] An internal calibration system consisting of a pair of ambient and heated blackbody targets is integrated into the PSR. Periodic views of these targets enable calibration of the PSR orthogonally polarized channels using a conventional two-look two-point method. The linearly polarized calibration standard used was similar to that described in [11], being comprised of hot and cold blackbody targets and a polarizing wire grid. The hot target was at ambient temperature, whereas the cold target was immersed in liquid nitrogen. The polarizing grid is a rectangular Duroid microwave substrate of 0.40 mm $(0.0157'')$ thickness with 0.17-mm-thick (0.5 oz/ft^2) printed copper grid lines. The line widths were 0.15 mm, and the filling factor was 0.25. The grid was bonded to a 13-mm thick styrofoam slab for mechanical stability. Overall grid dimensions were 444 mm $\times$ 582 mm. The linearly polarized standard was rotatable around its vertical axis to any arbitrary angle θ, as recorded using a 12-bit angular encoder. Unpolarized cold and hot brightness temperatures were generated by either removing the grid or replacing it with a flat aluminum reflecting plate, respectively.

[1]See http://www.etl.noaa.gov/technology/psr.

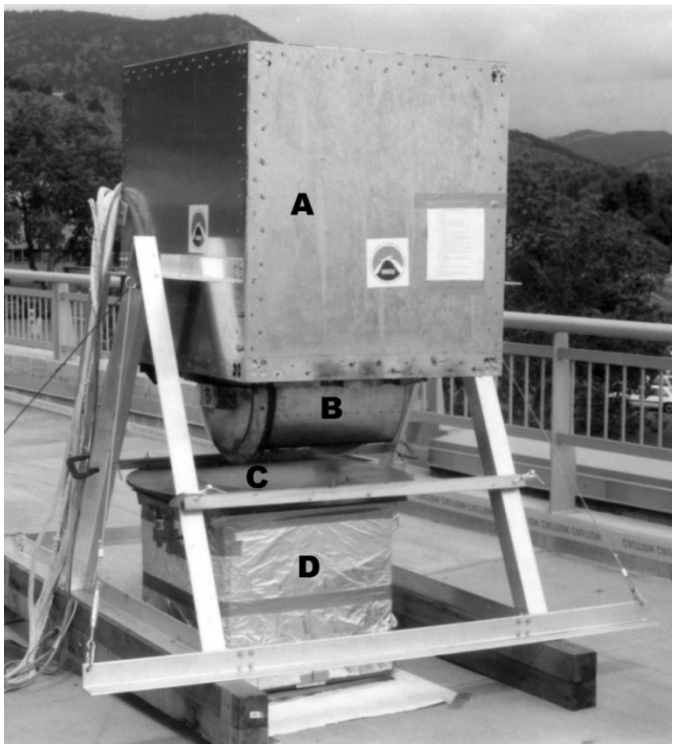

Fig. 2. NOAA fully polarimetric calibration experiment setup. (A) PSR housing, (B) PSR scanhead, (C) microwave retardation plate, and (D) linearly polarized standard.

The fully polarimetric standard was implemented by inserting a rotatable retardation plate over the aperture of the linearly polarized standard (Fig. 2). The retardation plate was fabricated out of a slab of cross-linked polystyrene (Rexolite 1422) with parallel grooves of spacing 5.07 mm, depth 15.12 mm, and fill factor 0.53, and machined on both faces (Fig. 3). The diameter of the aperture was 518 mm. The phase shift of the plate was determined by applying the formulas presented in [20] and [21] to be 53.4° at 10.7 GHz using the dielectric properties of Rexolite from [25] at 9.05 GHz ($\varepsilon_r' = 2.57$, $\varepsilon_r'' = 0.0013$). The plate's physical temperature was equal to the hot absorber temperature. Using flow graph network simulation, the power reflection of the plate at the applied frequency was estimated to be 1.9% and 1.0% for polarizations parallel and perpendicular to the slow axis, respectively. To minimize stray radiation leakage, the $\sim$140-mm-long gap between the antenna and the calibration standard was closed off using an aluminum foil shroud.

B. Measurements

The experiment consisted of a series of measurements using calibration standard configurations designed to provide a full rank observation matrix. The calibration standard was observed at a variety of rotation angles θ both with the retardation plate (i.e., for fully polarized observations) and without it (i.e., for purely linearly polarized observations). Cold and hot unpolarized observations were also made, both with and without the re-

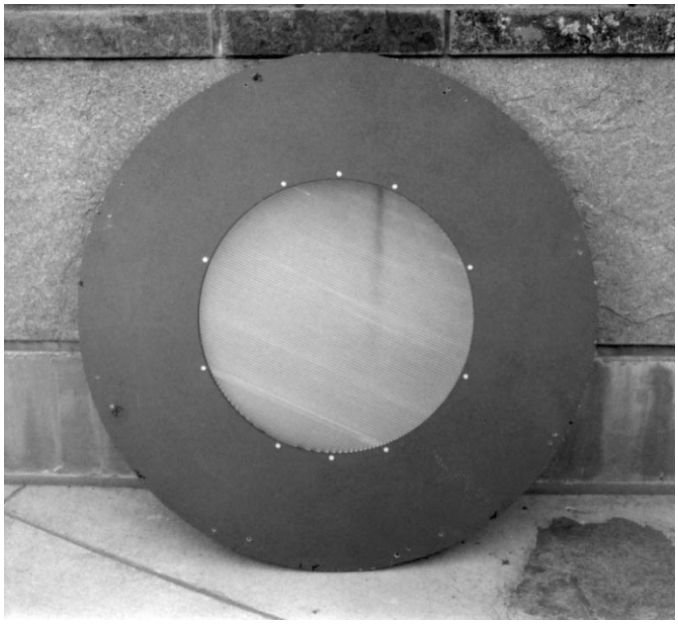

Fig. 3. Retardation plate of the NOAA/ETL fully polarimetric calibration standard; the plate is mounted on a wooden disk.

tardation plate. The retardation plate orientation angle φ was set to four distinct angles (-45°, 0°, 45°, and 90°), but otherwise remained invariant with respect to the antenna during rotation of the linearly polarized standard. The observed data were organized into sets obtained during one PSR internal calibration cycle. Each set consisted of several full rotations of the linearly polarized standard, with three to four such sets collected at each of the four retardation plate angles.

Parameters of the fully polarimetric standard were determined to calculate the generated *a priori* Stokes vectors using (5)–(22). The emissivity of the absorber material was considered to be essentially unity at the applied frequency range. The polarizing grid of the linearly polarized standard is etched on a low-loss microwave board, and it was thus unclear if the theoretical determination of freestanding wire grid characteristics as in [26] could be applied. Accordingly, values for $T'_{\rm HOT}$ and $T'_{\rm COLD}$ (which included the influence of the grid) were directly estimated by the orthogonal-channel data that were calibrated using PSR internal calibration targets. Measurements of the rotation angle θ were calibrated by finding the maxima and minima in the output signals of the orthogonal-channel polarizations.

The characteristics of the polarizing grid were studied without the retardation plate by varying θ. The orthogonal-channel signals were calibrated using PSR internal calibration targets. The brightness temperatures $T'_{\rm HOT}$ and $T'_{\rm COLD}$ were determined by applying (5) and (6) and pseudoinversion for the entire dataset. The estimated value of $T'_{\rm COLD}$ was compared with that obtained using a cold unpolarized view. No difference could be discerned. This indicates that the transmission and reflection characteristics of the grid were close to ideal and, thus, verify the feasibility of an etched polarizing grid for linearly polarized calibration standards.

The retardation plate losses were examined by measuring the unpolarized cold target through the plate. The plate caused less than a 2-K increase in brightness, indicating a combined reflection and absorption loss of less than 2%, and consistent with theoretical estimates.

C. Gain-Offset Estimation

The full gain-offset matrix was estimated for each observed dataset using (30). In order to obtain a sufficient number of linearly independent measurements, selected data for $\varphi = 90^\circ$ was incorporated with data for $\varphi = 0^\circ$, and vice versa. Similarly, selected data for $\varphi = 0^\circ$ was incorporated with data for $\varphi = -45^\circ$ and $\varphi = +45^\circ$. The PSR ambient internal calibration target was used as the unpolarized source. At 1° angular resolution the number of calibration looks ranged from 400 to 900 for each inversion. The *a priori* Stokes vectors for these sets were determined using (5)–(22). Two datasets are presented as examples: measurement "A" was performed with $\varphi = 90^\circ$, and measurement "B" with $\varphi = 45^\circ$. Raw voltages and calibrated responses for measurement "A" are shown in Figs. 4 and 5, respectively, and for measurement "B" in Figs. 6 and 7, respectively.

Comparing the calibrated brightness temperatures, it is seen that the amplitude modulation of the orthogonally polarized channels is much smaller for case "B" than for case "A". This reduction in amplitude is a consequence of the generation of quadrature-phased vertically and horizontally field components from the linearly polarized signal off the grid. Each of these field components has comparable brightness; therefore, the first two Stokes parameters are expected to be similar. The residual amplitude modulation is a consequence of the plate's phase shift being 53.4° (a 90° shift would cause no variation of T_v and T_h with θ). Another clear difference is that for case "B", the third and fourth Stokes parameters exhibit maxima that are offset by 45° in the angle θ. This is a consequence of the retardation plate not being parallel with one of the orthogonal polarizations of the antenna.

From the estimated gain matrix and offset vector for case "A"

$$\overline{\overline{g}} = \begin{bmatrix} 3600 & -67 & 2.8 & 2.1 \\ 200 & 7000 & -31 & 10 \\ 340 & 280 & 980 & -850 \\ 310 & 8.2 & 830 & 810 \end{bmatrix} \frac{\mu\text{V}}{\text{K}} \tag{45}$$

$$\overline{o} = \begin{bmatrix} -4.6 \\ -3.1 \\ -0.18 \\ 0.29 \end{bmatrix} \text{V} \tag{46}$$

several observations regarding the performance of the PSR 10.7-GHz radiometer (as aligned during this experiment) can be made. First, the symmetry of the gain elements g_{33}, g_{34}, g_{43}, and g_{44} indicate a significant ($\sim 45^\circ$) mixing between the third and fourth Stokes channels. Although this level of mixing is relatively large, it is also invertible in software (i.e., during calibration)—as evidenced by the positive determinant of the submatrix consisting of g_{33}, g_{34}, g_{43}, and g_{44}. Second, the mixing from the polarimetric channels (T_3 and T_4) into the orthogonal channels (T_v, T_h) is small, with brightness temperature errors in the orthogonal channels of order $\sim$0.02 K or less for a typical wind vector signal. Third, a significant level of orthogonal channel polarization mixing (from -15 to -17 dB)

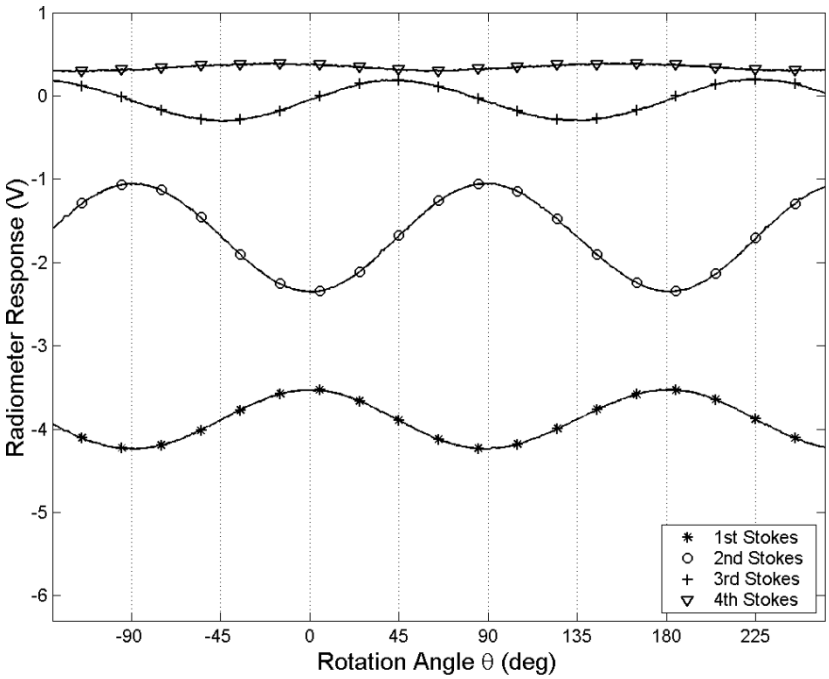

Fig. 4. Polarimetric response of the PSR 10.7-GHz channels as a function of linearly polarized standard rotation angle (θ). Measurement "A": $\varphi = 90°$.

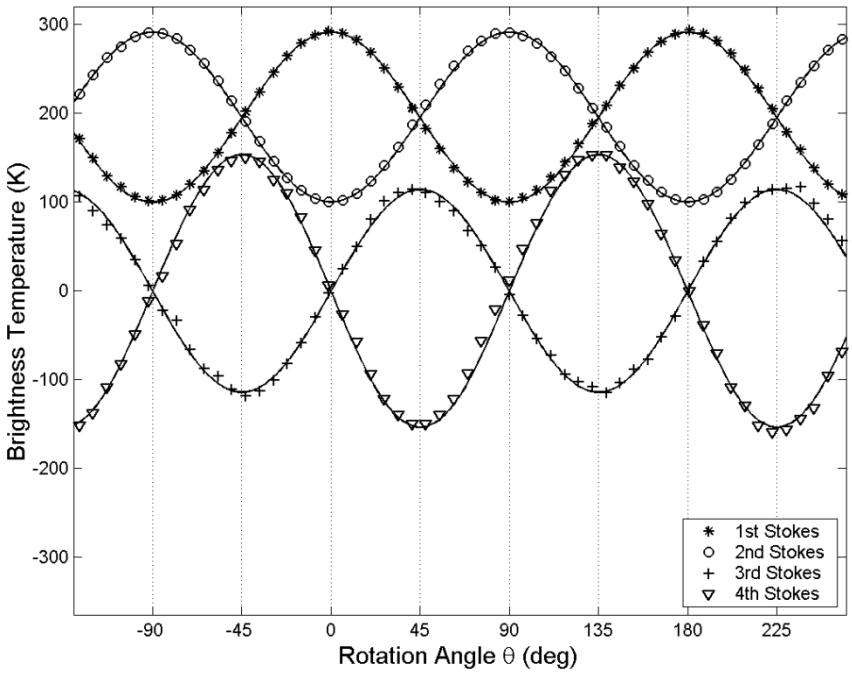

Fig. 5. Stokes parameters generated using the NOAA/ETL fully polarimetric calibration standard as a function of linearly polarized standard rotation angle (θ). Measurement "A": $\varphi = 90°$. The solid line represents the *a priori* brightness temperature, and the symbols the retrieved brightness temperature.

is apparent, but compensated in software by off-diagonal terms g_{12} and g_{21}.

D. Error Analysis

To determine calibration errors the random and systematic uncertainties in $\overline{T}_C$ were derived from the estimated uncertainties of the calibration standard parameters listed in Table II. The estimated uncertainty limits of Rexolite were set conservatively at $\Delta\varepsilon_r' = 0.02$, $\Delta\varepsilon_r'' = 0.0003$. The retardation plate manufacturing tolerances were estimated to be 25 μm. The uncertainty in the retardation plate phase shift was subsequently determined using standard propagation of errors. We note that an accurate figure for phase shift can also be obtained by direct measurement, e.g., as in [20]. The effect of nonzero bandwidth was computed and determined to be negligible.

The resulting gain-offset uncertainty matrix due to random uncertainty is obtained by (35), with relative gain and offset uncertainties during measurement "A" presented in (47) and (48),

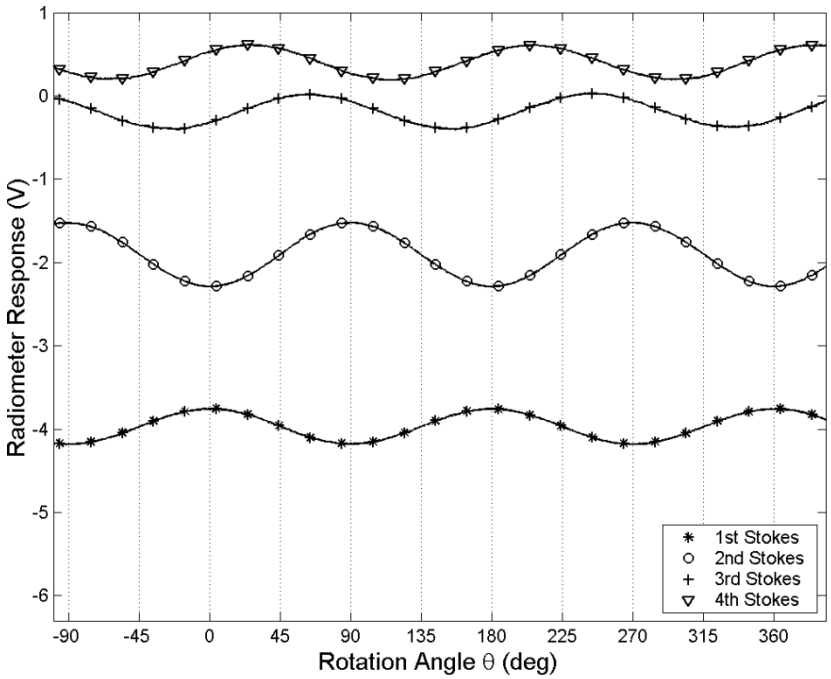

Fig. 6. Polarimetric response of the PSR 10.7-GHz channels as a function of linearly polarized standard rotation angle (θ). Measurement "B": $\varphi = -45°$.

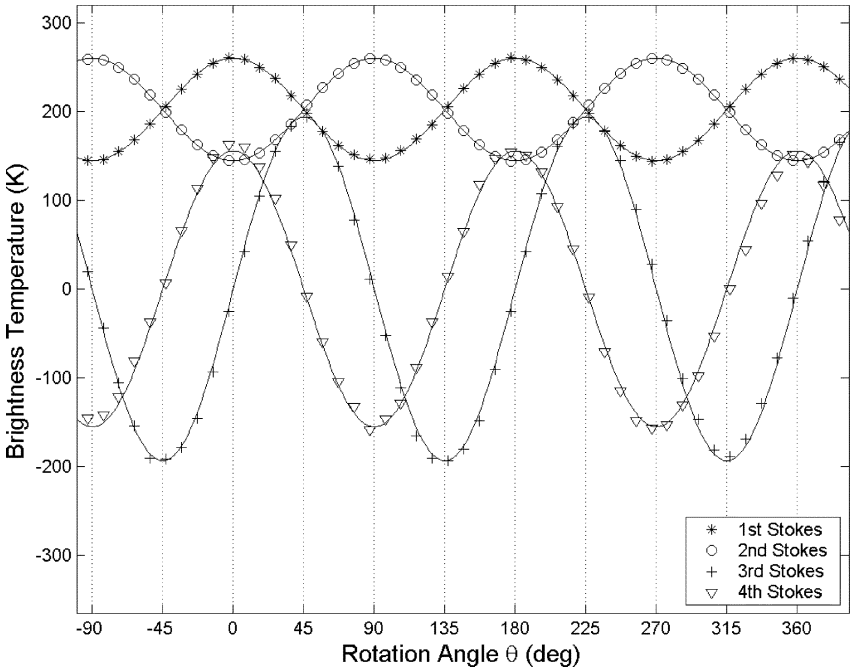

Fig. 7. Generated Stokes parameters by the NOAA/ETL fully polarimetric calibration standard as a function of linearly polarized standard rotation angle (θ). Measurement "B": $\varphi = -45°$. The solid line represents the *a priori* brightness temperature, symbols the retrieved brightness temperature.

respectively. The elements are normalized to the corresponding diagonal $g\alpha\alpha$ and $o\alpha$ elements, e.g., $\delta g_{\mathrm{REL},vh} = \langle \delta g_{vh}/g_{vv} \rangle$

$$\overline{\overline{\delta g}}_{\mathrm{REL}} = \begin{bmatrix} 0.4 & 0.4 & 2\cdot 10^{-4} & 1\cdot 10^{-4} \\ 0.4 & 0.4 & 1\cdot 10^{-4} & 1\cdot 10^{-4} \\ 2\cdot 10^{-2} & 1\cdot 10^{-2} & 7\cdot 10^{-3} & 5\cdot 10^{-3} \\ 2 & 2 & 2\cdot 10^{-2} & 2\cdot 10^{-2} \end{bmatrix} \% \quad (47)$$

$$\overline{\delta o}_{\mathrm{REL}} = \begin{bmatrix} 0.2 \\ 0.6 \\ 0.01 \\ 3 \end{bmatrix} \%. \quad (48)$$

As explained in Section II-C, radiometer biases due to systematic uncertainties of the calibration standard can be decreased *a posteriori*. The systematic uncertainties are therefore not considered within (47) and (48). For measurement "A", the correlation matrix of the diagonal elements of the gain-offset uncertainty matrix is obtained using (38)–(41)

$$\overline{\overline{r}}_{\left[\overline{\overline{\delta g}}_{\alpha\alpha} \quad \overline{\delta o}_{\alpha\alpha}\right]^T} = \begin{bmatrix} 1 & 0.25 & -0.22 & 0.22 & -0.79 \\ 0.25 & 1 & -0.50 & 0.50 & -0.79 \\ -0.22 & -0.50 & 1 & -1.00 & 0.46 \\ 0.22 & 0.50 & -1.00 & 1 & -0.46 \\ -0.79 & -0.79 & 0.46 & -0.46 & 1 \end{bmatrix}. \quad (49)$$

TABLE II
ESTIMATED UNCERTAINTIES FOR VARIOUS PARAMETERS OF THE NOAA/ETL FULLY POLARIMETRIC CALIBRATION STANDARD

Calibration Standard Parameter	T_{HOT}' (K)	T_{COLD}' (K)	T_{UP} (K)	T_R (K)	θ (deg)	φ (deg)	ζ (deg)	$l_\parallel$	$l_\perp$
Random Uncertainty	1	1	0.1	2	0.3	0.5	-	-	-
Systematic Uncertainty	1	1	1	5	0.2	1	1	$5.2\cdot10^{-4}$	$2.7\cdot10^{-4}$

The above matrix represents the degree by which random errors in the calibration standard impact the simultaneous determination of the gain-offset matrix elements.

IV. APPLICATION TO WIND VECTOR MEASUREMENTS

A promising application of airborne and spaceborne polarimetric radiometry is near-surface wind vector imaging (e.g., see [4]) for which the impact of absolute radiometric accuracy can be analyzed. As a benchmark set of wind vector accuracy requirements, we use the criteria proposed for the U.S. National Polar Orbiting Environmental Satellite System (NPOESS), for which a mandatory rms wind direction accuracy of 20° for wind speeds greater than 5 m/s has been specified, and with 10° as a goal [27]. Adopting these error thresholds, and using the satellite simulation results provided in [13], the maximum tolerable radiometer noise ΔT_α per beam footprint becomes ~1.2 K and ~0.8 K for the 20° and 10° rms direction accuracies, respectively. The above noise limit assumes a 10.7-, 18.7-, and 37-GHz tripolarimetric (T_v, T_h, and T_3) single-look radiometer and clear sky conditions.

We can now determine the impact of biases generated in the calibration process on wind direction estimation. Assuming the above directional accuracies (20° and 10°) as tolerable for the retrieved wind direction product, the resulting maximum biases in the T_3 or T_4 are determined from the mean slope of the azimuthal brightness harmonic functions

$$T_3 \approx b_{31} \cdot \sin(\phi_W) + b_{32} \cdot \sin(2\phi_W) \tag{50}$$

$$T_4 \approx b_{41} \cdot \sin(\phi_W) + b_{42} \cdot \sin(2\phi_W) \tag{51}$$

where ϕ_W is the look angle relative to the upwind direction. A model for b_{31} and b_{32} as a function of wind speed has been presented in [4] for a 53° incidence angle. The mean absolute values of $dT_3/d\phi_W$, i.e., $\langle |dT_3/d\phi_W| \rangle$ are ~0.006 K·deg^{-1} and ~0.005 K · deg^{-1} for 37 and 10.7 GHz, respectively, for 5 m/s wind speed. For 20° and 10° wind direction biases, we can thus tolerate no greater than ~0.12- K and ~0.06- K brightness bias, respectively, at 37 GHz, and ~0.10 K and ~0.05 K, respectively, at 10.7 GHz. These bias estimates assume low wind speeds and the use of only a single radiometer channel at a time, and thus are conservative. At higher wind speeds, and combining multiple radiometer channels these bias limits could be relaxed somewhat. For example, at 20-m/s wind speed, the bias limits for 20° and 10° wind direction biases are 0.41 and 0.21 K, respectively, at 37 GHz, and 0.46 and 0.23 K, respectively, at 10.7 GHz.

The biases generated as a result of calibration uncertainties, defined by (36) can now be compared to those computed above. A three-frequency (10.7, 18.7, and 37 GHz) spaceborne fully polarimetric radiometer observing at 53° from nadir is assumed along with a potential state-of-the-art fully polarimetric calibration system and a simplified calibration sequence as in Table I. Cold space at 2.73 K, known with high accuracy, is assumed for the cold blackbody target. The mean values of oceanic brightnesses over a full 360° of relative wind direction were modeled according to [4] and [28], with atmospheric corrections based on [29].

We can now estimate the calibration uncertainties in the case of this simplified calibration sequence on the three-band wind vector radiometer. The assumed random and systematic uncertainties of various calibration standard parameters are presented in Table III. The estimated systematic uncertainties of the hot target and unpolarized target brightness temperatures ($\sigma_{S,T_{B,\mathrm{HOT}}}$ and $\sigma_{S,T_{B,\mathrm{UP}}}$, respectively) are based on results presented in [22]. The values for $\sigma_{t_\parallel}$ and $\sigma_{r_\parallel}$ are based on [26], [30], and [31], with $L = 1 - r_\parallel - t_\perp$. We further assume that the phase shift of a single retardation plate increases linearly with frequency. In order to avoid the phase shift from being close to 0°, 90°, or 180° at any band, a value of 35.0° was selected for 10.7 GHz; the phase shift values for 18.7 and 37 GHz then follow to be 61.2°, and 121.0°, respectively. Note that the selected phase shift combination represents only one specific example; other phase shift combinations are possible but would alter the generated brightness temperature errors ΔT_3 and ΔT_4. We note that using $\zeta = 45°$ makes these errors equal, and larger values (between 45° and 90°) lead to an increase in ΔT_3 and a decrease in ΔT_4. Retardation plate reflections are also not considered here.

The brightness temperature errors caused by the above parameter uncertainties are presented in Table III; components smaller than 0.01 K are neglected. It can be seen that for the orthogonal channels the most significant sources of random error are those found in determining the absolute temperatures of fabricated blackbody targets. The most significant systematic error sources are the temperature of the hot target and the accuracy of the transmission and reflection parameters of the polarizing grid. For the polarimetric channels the most significant random and systematic error sources are the uncertainties in the rotation angles of the linearly polarized standard and the retardation plate. Note that potential reductions in random error due to an overdetermined calibration configuration set are not considered, so these calculations are considered conservative. The fact that T_v is more sensitive to uncertainty of the hot target brightness temperature than T_h is due to the higher vertical brightness temperatures observed over water.

As discussed earlier, radiometric biases due to systematic uncertainties incurred by the use of the fully polarimetric calibration system can be removed *a posteriori*, and are thus of less interest than those caused by random parameters. The errors

TABLE III
ESTIMATED UNCERTAINTIES OF A POTENTIAL STATE-OF-THE-ART CALIBRATION STANDARD AND THE GENERATED ERRORS OF ANTICIPATED OCEANIC BRIGHTNESS TEMPERATURES AT 10.7, 18.7, AND 37 GHz, ASSUMING THE CALIBRATION SEQUENCE OF TABLE I. THE GENERATED ERRORS DUE TO RANDOM, SYSTEMATIC, AND BOTH RANDOM AND SYSTEMATIC UNCERTAINTIES ARE DENOTED BY ΔT_R, ΔT_S, ΔT_{R+S}, RESPECTIVELY. A WIND SPEED OF 5 M/S AND CLEAR AIR IS ASSUMED. [a] AT 10.7, 18.7, AND 37 GHz

Calibration Standard Parameter	Uncertainty of the Parameter	Error of the Measured Stokes Parameters			
	Random Uncertainty	ΔT_v (K) [a]	ΔT_h (K) [a]	ΔT_3 (K) [a]	ΔT_4 (K) [a]
T_{HOT}	0.1 K	0.07/0.06/0.05	0.04/0.03/0.03	-	-
T_{UP}	0.1 K	0.01/0.01/0.02	0.01/0.01/0.02	-	-
T_R	0.1 K	-	-	-	-
T_G	0.1 K	-	-	-	-
θ	0.02°	-	-	0.18/0.09/0.08	0.13/0.17/0.13
φ	0.02°	-	-	0.04/0.10/0.23	0.13/0.17/0.13
Total Random Error, ΔT_R		**0.07/0.06/0.06**	**0.04/0.03/0.03**	**0.19/0.13/0.25**	**0.18/0.24/0.19**
Systematic Uncertainty					
T_{HOT}	0.2 K	0.14/0.12/0.10	0.08/0.07/0.05	-	-
T_{COLD}	0.01 K	-	-	-	-
T_{UP}	0.2 K	0.02/0.01/0.05	0.02/0.01/0.05	-	-
T_R	0.2 K	-	-	-	-
T_G	0.2 K	-	-	-	-
θ	0.02°	-	-	0.18/0.09/0.08	0.13/0.17/0.13
φ	0.02°	-	-	0.04/0.10/0.23	0.13/0.17/0.13
ζ	0.2°	-	-	-	-
$t_{\parallel} = r_{\perp}$	0.001	0.19/0.16/0.14	0.13/0.11/0.09	-	-
$r_{\parallel} = t_{\perp}$	0.001	0.13/0.11/0.09	0.19/0.16/0.14	-	-
$l_{\parallel}$	$3 \cdot 10^{-4}$	0.07/0.06/0.04	-	-	-
$l_{\perp}$	$1.5 \cdot 10^{-4}$	-	0.06/0.05/0.04	-	-
Total Systematic Error, ΔT_S		**0.28/0.24/0.20**	**0.25/0.22/0.18**	**0.19/0.13/0.25**	**0.18/0.24/0.19**
Resulted Total Error, ΔT_{R+S}		**0.29/0.25/0.21**	**0.25/0.22/0.18**	**0.26/0.19/0.35**	**0.25/0.33/0.26**

generated by random parameter uncertainties for the calibration sequence in Table I are seen to be low enough for wind vector measurements: these uncertainties are less than 0.1 K for the orthogonal polarizations and 0.1–0.3 K for the third and fourth Stokes parameters. Moreover, these random uncertainties are further diminished by increasing the number of calibration views at distinct values of θ and φ. By doing so the random errors fall within the prescribed NPOESS limits for T_3 at 10.7, 18.7, and 37 GHz. Provided that the calibration uncertainties are reasonably uncorrelated between channels and polarizations the impacts of these uncertainties are further reduced by $\sim\sqrt{N}$, where N is the number of polarized channels. Inclusion of additional calibration scenes without the retardation plate (i.e., tripolarimetric calibration) [21], optimizing the phase shift combination of the retardation plate at different frequencies, and removal of the remaining offset using the assumption $\langle T_3(\phi_W)\rangle \sim \langle T_4(\phi_W)\rangle \sim 0$ are additional means of random error reduction and should be considered.

We note that the set of calibration views chosen significantly impacts the ultimate calibration accuracy. For the orthogonally polarized channels alone this optimum set differs from that for the third and fourth Stokes parameters. The applied set of configurations should thus be optimized by taking several factors into consideration, including the importance of the individual Stokes parameters in the final product, the specific calibration parameter uncertainties, duration of the calibration, and other practical concerns such as radiometer stability.

Other issues associated with fully polarimetric calibration have also been considered. The loss of Rexolite material increases with increasing frequency. Although this effect was not taken into consideration in determining the brightness temperature uncertainties at 18.7 and 37 GHz, the influence of loss is very small and can be neglected. The impact of nonzero radiometric bandwidth was also considered. The radiometer was assumed to have rectangular passband with bandwidth of 2000 MHz at all frequencies. The resulting full-passband error using the selected phase shift values of the retardation plate was determined to be less than 0.001 K, and thus negligible.

V. SUMMARY

The conventional hot and cold blackbody technique that is widely used to calibrate conventional orthogonally polarized microwave radiometers is inadequate to calibrate modern polarimetric radiometers. The calibration system and application technique described herein is an extension of that of a linearly polarized standard [11] and fulfills the more extensive requirements of fully polarimetric calibration by presenting to the radiometer a precisely known set of polarized Stokes vectors. The system is based on a GK linearly polarized standard and a precision dielectric retardation plate. This study has presented the theoretical background for the fully polarimetric calibration system, including the mathematics necessary to

determine the *a priori* Stokes vectors, a calibration matrix inversion technique, and error analysis.

The application of the system was demonstrated in an experiment using the NOAA/ETL fully polarimetric calibration standard and Polarimetric Scanning Radiometer. During the experiment, the fully polarimetric gain and offset matrices and other parameters of PSR 10.7-GHz receiver were successfully identified. The uncertainties resulting from the use of a fully polarimetric calibration standard were also estimated. Using an anticipated oceanic brightness temperature scene, the applicability of the calibration system to wind vector radiometry was studied, and critical issues discussed. Specifically, it was shown that the NPOESS brightness accuracy requirements prescribed for wind vector measurements could be achieved using a potential state-of-the-art fully polarimetric calibration system based on the principles discussed herein.

APPENDIX

The vertical brightness temperature after the retardation plate ($T_{Cv,0}$) is obtained using the derivation in [18]

$$\begin{aligned} T_{Cv,0} &= \frac{\lambda^2 \cdot \left\langle |E_v|^2 \right\rangle}{k_B \cdot \eta} \\ &= [Q_{1v} + Q_{2v}\cos(2\varphi) + Q_{3v}\cos(4\varphi) \\ &\quad + Q_{4v}\sin(2\varphi) + Q_{5v}\sin(4\varphi)] \end{aligned} \tag{A1}$$

where

$$Q_{1v} = T_v \underbrace{\left[\frac{3}{8}\left(\frac{1}{l_\parallel^2}+\frac{1}{l_\perp^2}\right)+\frac{1}{4}\frac{\cos(\zeta)}{l_\parallel l_\perp}\right]}_{D_{v11}} + T_h \underbrace{\left[\frac{1}{8}\left(\frac{1}{l_\parallel^2}+\frac{1}{l_\perp^2}\right)-\frac{1}{4}\frac{\cos(\zeta)}{l_\parallel l_\perp}\right]}_{D_{v21}} \tag{A2}$$

$$Q_{2v} = T_v \underbrace{\frac{1}{2}\left(\frac{1}{l_\parallel^2}-\frac{1}{l_\perp^2}\right)}_{D_{v12}} \tag{A3}$$

$$Q_{3v} = T_v \underbrace{\frac{1}{8}\left[\frac{1}{l_\parallel^2}+\frac{1}{l_\perp^2}-2\frac{\cos(\zeta)}{l_\parallel l_\perp}\right]}_{D_{v13}} + T_h \underbrace{\frac{1}{8}\left[2\frac{\cos(\zeta)}{l_\parallel l_\perp}-\frac{1}{l_\parallel^2}-\frac{1}{l_\perp^2}\right]}_{D_{v23}} \tag{A4}$$

$$Q_{4v} = T_3 \underbrace{\frac{1}{4}\left(\frac{1}{l_\parallel^2}-\frac{1}{l_\perp^2}\right)}_{D_{v34}} + T_4 \underbrace{\frac{1}{2l_\parallel l_\perp}\sin(\zeta)}_{D_{v44}} \tag{A5}$$

$$Q_{5v} = T_3 \underbrace{\frac{1}{8}\left[\frac{1}{l_\parallel^2}+\frac{1}{l_\perp^2}-2\frac{\cos(\zeta)}{l_\parallel l_\perp}\right]}_{D_{v35}}. \tag{A6}$$

Similarly, the horizontal brightness temperature after the retardation plate ($T_{Ch,0}$) is obtained by

$$\begin{aligned} T_{Ch,0} &= \frac{\lambda^2 \cdot \left\langle |E_h|^2 \right\rangle}{k_B \cdot \eta} \\ &= [Q_{1h} + Q_{2h}\cos(2\varphi) + Q_{3h}\cos(4\varphi) \\ &\quad + Q_{4h}\sin(2\varphi) + Q_{5h}\sin(4\varphi)] \end{aligned} \tag{A7}$$

where

$$Q_{1h} = T_v \underbrace{\left[\frac{1}{8}\left(\frac{1}{l_\parallel^2}+\frac{1}{l_\perp^2}\right)-\frac{1}{4}\frac{\cos(\zeta)}{l_\parallel l_\perp}\right]}_{D_{h11}} + T_h \underbrace{\left[\frac{3}{8}\left(\frac{1}{l_\parallel^2}+\frac{1}{l_\perp^2}\right)+\frac{1}{4}\frac{\cos(\zeta)}{l_\parallel l_\perp}\right]}_{D_{h21}} \tag{A8}$$

$$Q_{2h} = T_h \underbrace{\frac{1}{2}\left(\frac{1}{l_\perp^2}-\frac{1}{l_\parallel^2}\right)}_{D_{h22}} \tag{A9}$$

$$Q_{3h} = T_v \underbrace{\frac{1}{8}\left[2\frac{\cos(\zeta)}{l_\parallel l_\perp}-\frac{1}{l_\parallel^2}-\frac{1}{l_\perp^2}\right]}_{D_{h13}} + T_h \underbrace{\frac{1}{8}\left[\frac{1}{l_\parallel^2}+\frac{1}{l_\perp^2}-2\frac{\cos(\zeta)}{l_\parallel l_\perp}\right]}_{D_{h23}} \tag{A10}$$

$$Q_{4h} = T_3 \underbrace{\frac{1}{4}\left(\frac{1}{l_\parallel^2}-\frac{1}{l_\perp^2}\right)}_{D_{h34}} + T_4 \underbrace{\frac{-1}{2l_\parallel l_\perp}\sin(\zeta)}_{D_{h44}} \tag{A11}$$

$$Q_{5h} = T_3 \underbrace{\frac{1}{8}\left[2\frac{\cos(\zeta)}{l_\parallel l_\perp}-\frac{1}{l_\parallel^2}-\frac{1}{l_\perp^2}\right]}_{D_{h35}}. \tag{A12}$$

The generated third and fourth Stokes parameters ($T_{C3,0}$ and $T_{C4,0}$) are derived by cross correlating the vertical and horizontal brightness temperatures [18]

$$\begin{aligned} T_{C3,0} &= 2\frac{\lambda^2}{k_B \cdot \eta} \cdot \mathrm{Re}\left\langle E_v E_h^* \right\rangle \\ &= [Q_{13} + Q_{23}\cos(2\varphi) + Q_{33}\cos(4\varphi) \\ &\quad + Q_{43}\sin(2\varphi) + Q_{53}\sin(4\varphi)] \end{aligned} \tag{A13}$$

$$Q_{13} = T_3 \underbrace{\frac{1}{4}\left[2\frac{\cos(\zeta)}{l_\perp l_\parallel}+\frac{1}{l_\parallel^2}+\frac{1}{l_\perp^2}\right]}_{D_{331}} \tag{A14}$$

$$Q_{23} = T_4 \underbrace{\frac{-1}{l_\perp l_\parallel}\sin(\zeta)}_{D_{342}} \tag{A15}$$

$$Q_{33} = T_3 \underbrace{\frac{1}{4}\left[2\frac{\cos(\zeta)}{l_\perp l_\parallel} - \frac{1}{l_\parallel^2} - \frac{1}{l_\perp^2}\right]}_{D_{333}} \tag{A16}$$

$$Q_{43} = T_v \underbrace{\frac{1}{2}\left(\frac{1}{l_\parallel^2} - \frac{1}{l_\perp^2}\right)}_{D_{314}} + T_h \underbrace{\frac{1}{2}\left(\frac{1}{l_\parallel^2} - \frac{1}{l_\perp^2}\right)}_{D_{324}} \tag{A17}$$

$$Q_{53} = T_v \underbrace{\frac{1}{4}\left[\frac{1}{l_\parallel^2} + \frac{1}{l_\perp^2} - 2\frac{\cos(\zeta)}{l_\perp l_\parallel}\right]}_{D_{315}} + T_h \underbrace{\frac{1}{4}\left[2\frac{\cos(\zeta)}{l_\perp l_\parallel} - \frac{1}{l_\parallel^2} - \frac{1}{l_\perp^2}\right]}_{D_{325}} \tag{A18}$$

$$\begin{aligned} T_{C4,0} &= 2\frac{\lambda^2}{k_B \cdot \eta} \cdot \operatorname{Im}\langle E_v E_h^* \rangle \\ &= [Q_{14} + Q_{24}\cos(2\varphi) + Q_{34}\sin(2\varphi)] \end{aligned} \tag{A19}$$

$$Q_{14} = T_4 \underbrace{\frac{\cos(\zeta)}{l_\perp l_\parallel}}_{D_{441}} \tag{A20}$$

$$Q_{24} = T_3 \underbrace{\frac{\sin(\zeta)}{l_\perp l_\parallel}}_{D_{432}} \tag{A21}$$

$$Q_{34} = T_v \underbrace{\left[\frac{-\sin(\zeta)}{l_\perp^2 l_\parallel^2}\right]}_{D_{414}} + T_h \underbrace{\frac{\sin(\zeta)}{l_\perp^2 l_\parallel^2}}_{D_{424}} \tag{A22}$$

ACKNOWLEDGMENT

The authors wish to thank the following individuals for their assistance: M. Hallikainen, M. Jacobson, V. Leuskiy, A. Yevgrafov, J. Praks, and J. Pulliainen. The support of S. Mango and R. Kakar is gratefully acknowledged.

REFERENCES

[1] V. S. Etkin, M. D. Raev, M. G. Bulatov, Y. A. Militsky, A. V. Smirnov, V. Y. Raizer, Y. A. Trokhimovsky, V. G. Irisov, A. V. Kuzmin, K. T. Litovchenko, E. A. Bespalova, E. I. Skvortsov, M. N. Pospelov, and A. I. Smirnov, "Radiohydrophysical aerospace research of ocean," Acad. Sciences, Space Res. Inst., Moscow, Russia, Rep. Π p-1749, 1991.

[2] V. G. Irisov, A. V. Kuzmin, M. N. Pospelov, J. G. Trokhimovsky, and V. S. Etkin, "The dependence of sea brightness temperature on surface wind direction and speed. Theory and experiment," in *Proc. IGARSS*, 1991, pp. 1297–1300.

[3] S. H. Yueh, W. J. Wilson, F. K. Li, S. V. Nghiem, and W. B. Ricketts, "Polarimetric measurements of sea surface brightness temperatures using an aircraft K-band radiometer," *IEEE Trans. Geosci. Remote Sensing*, vol. 33, pp. 85–92, Jan. 1995.

[4] J. R. Piepmeier and A. J. Gasiewski, "High-resolution passive polarimetric microwave mapping of ocean surface wind vector fields," *IEEE Trans. Geosci. Remote Sensing*, vol. 39, pp. 606–622, Mar. 2001.

[5] P. W. Rosenkranz and D. H. Staelin, "Polarized thermal microwave emission from oxygen in the mesosphere," *Radio Sci.*, vol. 23, pp. 721–729, Sept.–Oct. 1988.

[6] L. Tsang, J. A. Kong, and R. T. Shin, *Theory of Microwave Remote Sensing*. New York: Wiley, 1985.

[7] O. Koistinen, J. Lahtinen, and M. Hallikainen, "Comparison of analog continuum correlators for remote sensing and radio astronomy," *IEEE Trans. Instrum. Meas.*, vol. 51, pp. 227–234, Apr. 2002.

[8] J. R. Piepmeier and A. J. Gasiewski, "Digital correlation microwave polarimetry: Analysis and demonstration," *IEEE Trans. Geosci. Remote Sensing*, vol. 39, pp. 2392–2410, Nov. 2001.

[9] A. J. Gasiewski and D. B. Kunkee, "Polarized microwave thermal emission from water waves," *Radio Sci.*, vol. 29, no. 6, pp. 1449–1466, Nov.–Dec. 1994.

[10] K. M. St. Germain and P. W. Gaiser, "Spaceborne polarimetric microwave radiometry and the Coriolis windsat system," in *Proc. IEEE Aerospace Conf.*, vol. 5, 2000, pp. 159–164.

[11] A. J. Gasiewski and D. B. Kunkee, "Calibration and application of polarization-correlating radiometers," *IEEE Trans. Microwave Theory Tech.*, vol. 41, pp. 767–773, May 1993.

[12] W. N. Hardy, "Calibration and application to polarization correlating radiometers," *IEEE Trans. Microwave Theory Tech.*, vol. 21, pp. 149–150, Mar. 1973.

[13] J. R. Piepmeier, "Remote sensing of ocean wind vectors by passive microwave polarimetry," Ph.D. thesis, Georgia Inst. Technol., Atlanta, GA, 1999.

[14] S. J. Sharpe, A. J. Gasiewski, and D. M. Jackson, "Optimal calibration of radiometers using a multi-dimensional gain-offset Wiener filter," in *Proc. 1995 Progress in Electromagnetics Research Symp. (PIERS)*, 1995, p. 729.

[15] J. Lahtinen and M. Hallikainen, "Calibration of HUT polarimetric radiometer," in *Proc. IGARSS*, 1998, pp. 381–383.

[16] D. K. Cheng, *Fundamentals of Engineering Electromagnetics*. Reading, MA: Addison-Wesley, 1993.

[17] E. Salonen, "A Polarization measurement system for radio astronomical observations at the millimeter wave range," Licentiate thesis (in Finnish), Helsinki Univ. Technol., Espoo, Finland, 1986.

[18] J. Lahtinen, "Fully polarimetric radiometer system for airborne remote sensing," Dissertation thesis, Helsinki Univ. Technol., Espoo, Finland, to be published.

[19] A. H. F. van Vliet and T. de Graauw, "Quarter wave plates for submillimeter wavelengths," *Int. J. Inf. Millim. Waves*, vol. 2, no. 3, pp. 465–477, 1981.

[20] J. W. Lamb, A. V. Räisänen, and M. A. Tiuri, "Feed system for the Metsähovi cooled 75–95 GHz receiver," Helsinki Univ. Technol., Radio Lab., Espoo, Finland, Rep. S 146, 1983.

[21] J. Lahtinen and M. Hallikainen, "HUT fully polarimetric calibration standard for microwave radiometry," *IEEE Trans. Geosci. Remote Sensing*, vol. 41, Mar. 2003.

[22] D. M. Jackson, "Calibration of millimeter-wave radiometers with application to clear-air remote sensing of the amosphere," Ph.D. thesis, Georgia Inst. Technol., Atlanta, GA, 1999.

[23] G. Strang, *Linear Algebra and its Applications*. New York: Academic, 1976.

[24] J. Lahtinen and M. Hallikainen, "Fully polarimetric calibration system for HUT polarimetric radiometer," in *Proc. IGARSS*, 2000, pp. 1542–1544.

[25] L. C. Chen, C. K. Ong, and B. T. G. Tan, "Cavity perturbation technique for the measurement of permittivity tensor of uniaxially anisotropic dielectrics," *IEEE Trans. Instrum. Meas.*, vol. 48, pp. 1023–1030, Dec. 1999.

[26] W. G. Chambers, A. E. Costley, and T. J. Parker, "Characteristic curves for the spectroscopic performance of free-standing wire grids at millimeter and submillimeter wavelengths," *Int. J. Inf. Millim. Waves*, vol. 9, no. 2, pp. 157–172, 1988.

[27] NOAA. (2000) Conical Scanning Microwave Imager/Sounder (CMIS), Sensor Requirements Document (SRD) for National Polar-Orbiting Environmental Satellite System (NPOESS) Spacecraft and Sensors, Version Two. Associate Directorate for Acquisition NPOESS Integrated Program Office, Silver Spring, MD. [Online]. Available: http://npoesslib.ipo.noaa.gov/SRD/CMIS/CMIS-web-Ver2-0800.pdf

[28] P. Schluessel and H. Luthard, "Surface wind speeds over the north sea from special sensor microwave/imager observations," *J. Geophys. Res.*, vol. 96, no. C3, pp. 4845–4853, 1991.

[29] F. Ulaby, R. Moore, and A. Fung, *Microwave Remote Sensing, Active and Passive*. Reading, MA: Artech House, 1981, vol. I.

[30] A. A. Volkov, B. P. Gorshunov, A. A. Irisov, G. V. Kozlov, and S. P. Lebedev, "Electrodynamic properties of plane wire grids," *Int. J. Inf. Millim. Waves*, vol. 3, no. 1, pp. 19–43, 1982.

[31] J. Lahtinen and M. Hallikainen, "Fabrication and characterization of large free-standing polarizer grids for millimeter waves," *Int. J. Inf. Millim. Waves*, vol. 20, no. 1, pp. 3–20, Jan. 1999.

Janne Lahtinen (S'98) received the M.S. (Tech.) and Lic. Sci. (Tech.) degrees from the Helsinki University of Technology (HUT), Espoo, Finland, in 1996 and 2001, respectively.

He is currently a Research Fellow at the European Space Agency's European Research and Technology Centre (ESTEC), Noordwijk, The Netherlands. From 1995 to 2002, he was with the HUT Laboratory of Space Technology. His research has focused on microwave radiometer systems, with emphasis on polarimetric and interferometric radiometers. He has authored and coauthored more than 20 publications in the area of microwave remote sensing.

Mr. Lahtinen received the third place in the IEEE Geoscience and Remote Sensing Society Student Prize Paper Competition in 2000, and he won the Young Scientist Award of the Finnish National Convention on Radio Science in 2001. He served as a Secretary of the Finnish National Committee of COSPAR from 1997 to 2002 and as a Secretary of the Space Science Committee, appointed by Finnish Ministry of Education, from 1999 to 2000.

A. J. Gasiewski (S'81–M'88–SM'95–F'02) received the M.S. and B.S. degrees in electrical engineering and the B.S. degree in mathematics, all from Case Western Reserve University, Cleveland, OH, in 1983, and the Ph.D. degree in electrical engineering and computer science from the Massachusetts Institute of Technology, Cambridge, in 1989.

From 1989 to 1997, he was Faculty Member within the School of Electrical and Computer Engineering, Georgia Institute of Technology (Georgia Tech), Atlanta. As an Associate Professor at Georgia Tech, he developed and taught courses on electromagnetics, remote sensing, instrumentation, and wave propagation theory. He is currently with the U.S. National Oceanic and Atmospheric Administration's (NOAA) Environmental Technology Laboratory (ETL) in Boulder, CO, where he is Acting Chief of the ETL Microwave Systems Development Division. His technical interests include passive and active remote sensing, radiative transfer theory, electromagnetics, antennas and microwave circuits, electronic instrumentation, meteorology, and oceanography.

Dr. Gasiewski is currently Executive Vice President of the IEEE Geoscience and Remote Sensing Society and was General Chair of the 2nd Combined Optical-Microwave Earth and Atmosphere Sensing Symposium (CO-MEAS 1995). He organized the technical program for the 20th International Geoscience and Remote Sensing Symposium (IGARSS 2000) and is the named General Co-Chair of IGARSS 2006, to be held in Denver, CO. He is a member of Tau Beta Pi, Sigma Xi, the American Meteorological Society, the American Geophysical Union, and the International Union of Radio Scientists (URSI). He is currently serving as secretary of USNC/URSI Commission F. He has served on the U.S. National Research Council's Committee on Radio Frequencies (CORF) from 1989 to 1995.

Marian Klein received the M.S. and Ph.D. degrees in electrical engineering from the Technical University of Kosice (TU Kosice), Kosice, Slovak Republic, in 1986 and 1996, respectively.

He is currently a Group Leader in microwave radiometry at the National Oceanic and Atmospheric Administration, Environmental Technology Laboratory, Boulder, CO. From 1987 to 1996, he was a faculty member within the Faculty of Electrical Engineering and Informatics at the TU Kosice. From September 1996 to June 1997, he was a Fulbright Scholar at the Georgia Institute of Technology, Atlanta, working in the Laboratory for Radio Science and Remote Sensing. From June 1997 to August 1998, he was a Guest Worker at the National Oceanic and Atmospheric Administration, Environmental Technology Laboratory. From 1998 to 2002, he was with the Cooperative Institute for Research in Environmental Sciences, University of Colorado, Boulder. His areas of technical expertise include passive microwave remote sensing and radiative transfer theory.

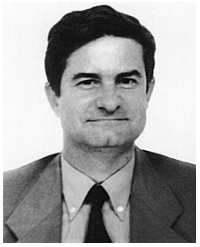

Ignasi S. Corbella (M'99) received the Enginyer and Doctor Enginyer degrees in telecommunication engineering, both from the Universitat Politècnica de Catalunya (UPC), Barcelona, Spain, in 1977 and 1983, respectively.

He is currently teaching microwaves at the undergraduate level at UPC and has designed and taught graduate courses on nonlinear microwave circuits. In 1976, he joined the School of Telecommunication Engineering, UPC, as a Research Assistant in the Microwave Laboratory, were he worked on passive microwave integrated circuit design and characterization. He worked at Thomson-CSF, Paris, France on microwave oscillators design in 1979. He was an Assistant Professor at UPC in 1982, Associate Professor in 1986, and Full Professor in 1993. During the school year 1998 to 1999, he worked at the National Oceanic and Atmospheric Administration, Environmental Technology Laboratory, Boulder, CO, as a Guest Researcher, where he developed methods for radiometer calibration and data analysis. His research work in the Department of Signal Theory and Communications, UPC includes microwave airborne and satellite radiometry and microwave system design and is at present Director of the department.